

1 **Revision 3**

2 **Amorphous Mn<sub>2</sub>SiO<sub>4</sub>: A potential manganese phase in the stagnant slab**

3 Zhilin Ye <sup>1,2</sup>, Jingui Xu <sup>1,3,\*</sup>, Dawei Fan <sup>1,\*</sup>, Dongzhou Zhang <sup>3</sup>, Wenge Zhou <sup>1</sup>,

4 Hongsen Xie <sup>1</sup>

5 1 Key Laboratory of High-Temperature and High-Pressure Study of the Earth's  
6 Interior, Institute of Geochemistry, Chinese Academy of Sciences, Guiyang, Guizhou  
7 550081, China

8 2 University of Chinese Academy of Sciences, Beijing 100049, China

9 3 Hawaii Institute of Geophysics and Planetology, School of Ocean and Earth Science  
10 and Technology, University of Hawaii at Manoa, Honolulu, Hawaii 96822, USA

11 \* Corresponding authors:

12 **E-mail addresses:** [fandawei@vip.gyig.ac.cn](mailto:fandawei@vip.gyig.ac.cn) (D. Fan), [xujingui1990@126.com](mailto:xujingui1990@126.com) (J.  
13 Xu)

14

15 **Keywords:** Tephroite, Amorphization, Single-crystal X-ray diffraction, High-pressure  
16 Raman spectra, Stagnant slab

17

18 **Abstract**

19 Tephroite (Mn<sub>2</sub>SiO<sub>4</sub>), together with some manganese (Mn)-rich mineral inclusions,  
20 has been found in ophiolite-hosted diamonds, possibly originating from Mn-nodules  
21 and sediments that were once deposited on the oceanic floor and later subducted into  
22 the deep mantle, which provides evidence for oceanic crustal recycling. However, the

23 state and behaviors of tephroite under high-pressure and high-temperature conditions  
24 remain poorly understood. In this study, we conducted *in situ* synchrotron  
25 single-crystal X-ray diffraction (XRD) and Raman spectroscopy of synthetic tephroite  
26 up to ~30 GPa and ~900 K. The XRD and Raman spectroscopy experiments in this  
27 study firstly show that tephroite undergoes pressure-induced irreversible amorphous  
28 transformation above ~20 GPa. Temperature (< 900 K) is found to not be an important  
29 factor controlling the process of amorphous transformation. Amorphous tephroite may  
30 be a potential phase in a rapidly cooling oceanic lithospheric subduction slab  
31 stagnating at the bottom of the mantle transition zone.

32

### 33 **Introduction**

34 Olivine, the most dominant mineral in the Earth's mantle, is an important  
35 substitutional solid-solution silicate composed of end-member forsterite ( $\text{Mg}_2\text{SiO}_4$ )  
36 and fayalite ( $\text{Fe}_2\text{SiO}_4$ ) (Ringwood 1991). It is also found in igneous and metamorphic  
37 rocks, meteorites, and many other extraterrestrial environments (Mason 1963; Nguyen  
38 and Zinner 2004; Mustard et al. 2005; Zolensky et al. 2006; Finkelstein et al. 2014).  
39 In addition, other end-member olivines composed of transition metal ions (*e.g.*,  
40 tephroite ( $\text{Mn}_2\text{SiO}_4$ ) and libenbergitite ( $\text{Ni}_2\text{SiO}_4$ )) are found in nature. Even a small  
41 concentration of transition metals can profoundly influence the optical, magnetic, and  
42 transparency properties and thermodynamic behaviors of crystals (Geiger et al. 2019).  
43 The existence of transition metal elements also affects large-scale geodynamic  
44 processes such as redox reactions and deep mantle melting on Earth (Gaillard et al.

45 2015).

46 Recently, tephroite associated with other manganese (Mn)-rich minerals, such as  
47 spessartite (Mn garnet),  $(\text{Ca, Mn})\text{SiO}_3$ -perovskite, MnO, and NiMnCo alloy, was  
48 discovered in ophiolite-hosted diamonds (Yang et al. 2015a, 2015b; Lian et al. 2018;  
49 Lian and Yang 2019), which has never been found in other diamonds. These  
50 significant ranges of ultrahigh-pressure (UHP) and highly reduced inclusions in  
51 ophiolite-hosted diamonds reflect a completely new environment for diamond  
52 formation in the mantle. It is suggested that these minerals may be a common feature  
53 of the *in situ* oceanic lithosphere (Yang et al. 2015b). Generally, Mn-rich olivine  
54 associated with iron-Mn ore deposits and skarns is formed by complex interactions in  
55 the ocean-atmosphere-lithosphere system (Cloutis 1997). However, research focused  
56 on the properties of tephroite under high-pressure and high-temperature conditions is  
57 limited. Isomorphic forsterite and fayalite both undergo different phase transitions at  
58 high pressure and high temperature.  $\text{Mg}_2\text{SiO}_4$  transforms into wadsleyite (spinelloid  
59 structure) at 12-15 GPa and further transforms into ringwoodite (spinel structure) at  
60 ~18-20 GPa (Frost 2008), while  $\text{Fe}_2\text{SiO}_4$  transforms directly into a spinel structure at  
61 6-7 GPa. Moreover, pressure-induced amorphizations (PIAs) of forsterite and fayalite  
62 are observed at room temperature and higher pressures of 56-80 GPa (Jeanloz et al.  
63 1977; Guyot and Reynard 1992; Durben et al. 1993; Andrault et al. 1995; Rouquette  
64 et al. 2008; Santamaria-Perez et al. 2016; Kim et al. 2021) and ~35 GPa (Richard and  
65 Richet 1990; Williams et al. 1990; Andrault et al. 1995; Speziale et al. 2004),  
66 respectively. Recently, it has been proposed that amorphization takes place at the

67 forsterite grain boundary under stress, which can trigger a plastic process in the deep  
68 Earth and greatly affect the transition layer of the lithospheric transition zone (Samae  
69 et al. 2021).

70 However, the only study focused on the stability of tephroite indicates that  
71 tephroite does not undergo a spinelloid structure or spinel structure transformation  
72 like forsterite and fayalite, but decomposes into MnO (rock salt) and MnSiO<sub>3</sub>  
73 (tetragonal garnet-like structure) at  $P > 14$  GPa and  $T = 1273$  K and further into MnO  
74 and SiO<sub>2</sub> at higher pressure ( $P > 30$  GPa) (Ito et al. 1974). Whether tephroite  
75 undergoes a similar phase transformation or amorphization in a high-temperature and  
76 high-pressure range like forsterite and fayalite and what impact such a transformation  
77 are uncertain. Therefore, knowledge of the high-pressure and high-temperature  
78 behaviors of tephroite would help us to understand the occurrence of tephroite in the  
79 deep Earth and provide new insights into the process of its encapsulation in the  
80 diamond.

81 To address these issues, we investigated the stability of single-crystal tephroite  
82 through *in situ* synchrotron single-crystal X-ray diffraction (SCXRD) and Raman  
83 scattering experiments at high pressures and high temperatures, simulating conditions  
84 within the cold subducting lithosphere. The compressive equation of state, a  
85 compression mechanism, thermal stability, and PIA of tephroite are determined up to  
86  $\sim 30$  GPa and  $\sim 900$  K in this study. The results indicate that tephroite may be able to  
87 exist in the Earth's interior in an amorphous state and transform into crystalline  
88 phases on its way back to the surface by being wrapped in the diamond.

89

## 90 **Methods**

### 91 **Sample preparation**

92 The tephroite sample measured in this study was synthesized using high purity oxides  
93 (MnO, SiO<sub>2</sub>) in a multi-anvil high-pressure apparatus at 4.0 GPa and 1273 K for 36  
94 hours at the Institute of Geochemistry, Chinese Academy of Sciences, Guiyang, China.  
95 Electron microprobe analysis (EMPA) was carried out with an EMPA1600, operating  
96 at an acceleration voltage of 25 kV, beam current of 10 nA, and focused electron beam  
97 of approximately 5 μm, with which the chemical composition of the sample was  
98 determined to be Mn<sub>1.98</sub>Si<sub>0.98</sub>O<sub>4</sub> (Table S1).

### 99 ***In situ* single-crystal X-ray diffraction**

100 A 30×40 μm<sup>2</sup> fragment of single-crystal tephroite with a thickness of less than 15  
101 μm was mounted on a polymer holder used for room-pressure measurement. The  
102 high-pressure experimental samples were loaded in a symmetric-type DAC with ± 32°  
103 opening angles equipped with a pair of 400 μm culet-size diamond anvils, while the  
104 high-pressure and high-temperature experimental sample was loaded in a BX90  
105 externally heated diamond anvil cell (EHDAC) with ± 15° opening angles equipped  
106 with a pair of 500 μm culet-size diamond anvils. A resistive heater was used to  
107 generate a maximum temperature of 900 K, and the temperature was measured by a  
108 K-type thermocouple. The temperature of the experiment was raised from room  
109 temperature to a maximum temperature of 900 K at intervals of 200 K and then  
110 cooled to room temperature at the same interval. After pressurization at room

111 temperature, the same heating and cooling operation was conducted (Figure S1). The  
112 pressure was determined by the calibrated shift of the R1 ruby fluorescence band  
113 (Mao et al. 1986) for the high-pressure experiments and the equation of state of gold  
114 (Fei et al. 2007) for the high-pressure and high-temperature experiments. Neon was  
115 used as the pressure-transmitting medium (Rivers et al. 2008).

116 The *in-situ* synchrotron SCXRD experiments were conducted at experimental  
117 station 13-BM-C of the Advanced Photon Source at Argonne National Laboratory;  
118 more experimental details were previously described (Xu et al. 2020b; Ye et al. 2021).  
119 The Bruker APEX3 software package was used to analyze the diffraction images, and  
120 crystal refinements were carried out with the SHELXL and Olex2 software packages  
121 (Sheldrick 2008; Dolomanov et al. 2009), starting from the *Pbnm* structure modeled  
122 by Fujino et al. (1981) to initialize the refinement. All atoms in this study were  
123 modeled with isotropic atomic displacement parameters (*U*<sub>iso</sub>). The crystal structure  
124 of tephroite under ambient conditions is diagramed in Figure S2 by the VESTA  
125 program (Momma and Izumi 2011). The unit-cell parameters are shown in Table S2,  
126 and the refinement details can be seen in Table S3 and Table S4.

### 127 **Raman spectroscopy**

128 High-pressure Raman spectra were collected between 37-1300 cm<sup>-1</sup> using a Renishaw  
129 RM 1000 Raman microscope with a Peltier-cooled charge-coupled device (CCD)  
130 detector at the Center for High Pressure Science & Technology Advanced Research.  
131 Raman spectra were obtained using a 532 nm wavelength from the Ar<sup>+</sup> laser with a  
132 maximum spot of ~2 μm. The sample was focused through a Nikon L Plan EPI 20X

133 with a 0.35 objective. At each pressure step, the Raman spectrum was collected for a  
134 duration of 300 s. All spectra were obtained in the backscattering geometry with no  
135 polarization used for the collected signal. The Raman spectra were analyzed by  
136 Lorentzian curve fitting using the Peakfit program (Systat Software, San Jose, CA,  
137 USA).

138

## 139 **Results**

### 140 ***PVT* equation of state of tephroite**

141 During continuous pressurization to 29.9(2) GPa in the room-temperature and  
142 high-pressure experiment, SCXRD shows that tephroite retains the initial *Pbnm*  
143 olivine structure up to ~20 GPa (Table S1 and Figure S1). As shown in Figure 1, the  
144 SCXRD images reflect a phase transformation of tephroite characterized by  
145 conspicuous changes after ~20 GPa. The SCXRD images after phase transformation  
146 exhibit fewer peaks than those of the initial tephroite phase. The loss of sharp  
147 crystalline diffraction peaks indicates that tephroite undergoes PIA. This is the first  
148 time that tephroite has been observed to undergo amorphous transformation. Due to  
149 the occurrence of amorphization, unit-cell parameters and structural information of  
150 tephroite above 20 GPa cannot be obtained.

151 The *P-V* compression curve of the tephroite sample in the pressure range of 0-20  
152 GPa is fitted to the third-order Birch-Murnaghan Equation of State (BM3-EoS)  
153 (Birch 1947) using the EoSFit software package (Angel et al. 2014). The EoS  
154 parameters, including the zero-pressure volume ( $V_{T0}$ ), isothermal bulk modulus ( $K_{T0}$ ),

155 and its pressure derivative ( $K'_{T0}$ ), are obtained without any constraints. The best-fit  
156 parameters are:  $V_{T0} = 325.22(13)$  Å,  $K_{T0} = 124(1)$  GPa, and  $K'_{T0} = 4.67(29)$ . Compared  
157 with other end-member olivines, the bulk modulus of tephroite exhibits the most  
158 compressible (Table S5). The bulk modulus of transition metal olivine (Mn, Fe, Co,  
159 Ni)<sub>2</sub>SiO<sub>4</sub> decreases linearly with increasing ionic radius (Figure S3). The relationship  
160 between the Eulerian strain ( $f_E$ ) and normalized pressure ( $F_E$ ) shows a slightly positive  
161 slope (Figure 2a). The weighted linear fit of the  $f_E - F_E$  plot yields  $K_{T0}$  (124.3(8) GPa)  
162 and  $K'_{T0} > 4$ , which are in close agreement with those from the BM3-EoS fit,  
163 indicating that the BM3-EoS is suitable for fitting the high-pressure data. The axial  
164 compressibilities are also determined using the BM3-EoS (Figure S4 and Table S6).  
165 The ambient-pressure axial compressibility  $\beta_{l0}$  is defined as  $1/(3M_{l0})$ . At ambient  
166 pressure, the axial compressibilities of the three axes are  $\beta_{a0} = 6.03(16) \times 10^{-4}$  GPa<sup>-1</sup>,  
167  $\beta_{b0} = 1.22(2) \times 10^{-3}$  GPa<sup>-1</sup>, and  $\beta_{c0} = 9.78(37) \times 10^{-4}$  GPa<sup>-1</sup>. The ratio of the axial  
168 compressibility at ambient pressure is  $\beta_{a0} : \beta_{b0} : \beta_{c0} = 1.00 : 2.02 : 1.62$ . The tephroite  
169 crystal exhibits elastic anisotropy under compression, where the compressibility along  
170 the *b* axis is the highest. The relative axial compressibility of tephroite is comparable  
171 to that of other end-member olivines (Figure S4). To accurately account for the further  
172 understanding of compressional behavior under high pressure, we investigate  
173 polyhedral compression with pressure by crystal structure refinement. The pressure  
174 dependencies of polyhedral volumes and averaged bond length are shown in Figure  
175 S5 (a and b) and Figure S6.  
176 The high-pressure and high-temperature experiments yield the same results as the



177 room-temperature and high-pressure experiments; that is, tephroite becomes  
178 amorphous upon subsequent pressurization to 20 GPa at a temperature of 900 K. After  
179 the amorphous transformation, tephroite does not return to its initial crystal structure  
180 despite a drop in temperature or pressure from the highest temperature and pressure in  
181 this study (~900 K and ~25.5 GPa). Similar to the results of the room-temperature and  
182 high-pressure experiments, the pressure of the amorphous transformation of tephroite  
183 in the high-pressure and high-temperature experiments is approximately 20 GPa.  
184 Temperature does not have a conspicuous effect on the amorphous transformation.

185 The pressure-volume-temperature ( $P$ - $V$ - $T$ ) data of tephroite within 20 GPa are fitted  
186 by the high-temperature third-order Birch-Murnaghan equation of state  
187 (HT-BM3-EoS) (Birch 1947; Fei 1995) using the EoSFit software package (Angel et  
188 al. 2014) (Figure 2b). The obtained thermal EoS parameters are  $V_{T0} = 324.95(7)$  Å,  
189  $K_{T0} = 122.5$  GPa,  $K'_{T0} = 4.07(25)$ , the temperature derivative of the bulk modulus  
190  $(\partial K_T/\partial T)_P$  is  $-0.022(3)$  GPa·K<sup>-1</sup> and the thermal expansion at room pressure ( $\alpha_0$ ) is  
191  $4.20(17)\times 10^{-5}$  K<sup>-1</sup>.

## 192 **Raman spectra of tephroite at high pressures**

193 Olivine ( $M_2SiO_4$ ,  $M = Mg, Fe, Mn, Ni, Co$ ) with orthorhombic ( $Pbnm$ ) symmetry,  
194 belongs to the orthorhombic space group  $D_{2h}^{16}$  and contains four  $M_2SiO_4$  formula units  
195 in its primitive unit cell. The symmetry analysis of invariant atoms predicts 84  
196 vibrational modes in the structure of olivine, of which the 36 Raman-active  
197 vibrational modes are  $11A_g + 11B_{1g} + 7B_{2g} + 7B_{3g}$  (Chopelas 1991; Kolesov and  
198 Geiger 2004). The prominent two Raman peaks ( $\nu_1$  and  $\nu_3$ ) of olivine crystals are the

199 Si-O stretching mode produced by the coupled vibration of the SiO<sub>4</sub> tetrahedron  
200 between 800 and 1000 cm<sup>-1</sup> under ambient conditions.

201 The spectra of tephroite collected in this experiment are unpolarized (Figure 3),  
202 which ensures that the major peaks can be represented and that the wavenumbers of  
203 individual bands can be determined by Lorentzian curve fitting (Table S7). However,  
204 some bands shown in the polarized single-crystal spectrum are not observed in the  
205 spectrum obtained under ambient conditions. Thirteen of the 36 Raman-active  
206 vibrational modes of tephroite observed are distributed as follows (Figure 3):  
207 symmetric ( $\nu_1$ ) and asymmetric ( $\nu_3$ ) Si-O stretching modes of SiO<sub>4</sub><sup>+</sup> in the range of  
208 810-935 cm<sup>-1</sup>; symmetric ( $\nu_2$ ) and asymmetric ( $\nu_4$ ) O-Si-O bending modes between  
209 392-515 cm<sup>-1</sup>; and lattice vibrations involving translations of Mn<sup>2+</sup> as well as  
210 translations and vibrations of SiO<sub>4</sub> tetrahedra in the range of 243-317 cm<sup>-1</sup>.

211 The Raman spectra of a single-crystal sample of tephroite at high pressures are  
212 obtained by quasi-hydrostatic pressurization in a Ne pressure medium up to 29.1 GPa  
213 (Figure 3). The Raman-active modes shift toward higher frequencies with increasing  
214 pressure. The vibrational frequency is linearly fitted to the pressure, and the slopes of  
215  $(\partial\nu_i/\partial P)_T$  (cm<sup>-1</sup>/GPa) show that the frequencies increase at rates of 1.3-4.7 cm<sup>-1</sup>/GPa  
216 under pressurization (Figure 4). In the high-pressure experiment, the signal collected  
217 through the diamond windows becomes relatively weak, especially for lattice  
218 vibrations in the low-frequency range. The peaks at 276 cm<sup>-1</sup>, 287 cm<sup>-1</sup>, and 302 cm<sup>-1</sup>  
219 gradually become undetectable as the pressure increases. The principal Raman peaks  
220 show slight peak broadening and intensity weakening at ~21.3 GPa, accompanied by

221 the appearance of some new peaks at 244 cm<sup>-1</sup>, 622 cm<sup>-1</sup>, and 812 cm<sup>-1</sup> and loss of  
222 definition in the high-frequency modes. However, upon decompression, the  
223 pressure-induced phase transformation of tephroite does not turn to its initial structure.  
224 This phenomenon is extremely consistent with the results obtained by the SCXRD  
225 experiment in this study; that is, tephroite undergoes a pressure-induced amorphous  
226 phase transition at ~20 GPa.

227 The isothermal-mode Grüneisen parameters ( $\gamma_{iT}$ ) describe the variation in  $\nu_i$  with  
228 pressure at a constant temperature according to the following formula (Gillet and  
229 Guyot 1988):

$$230 \quad \gamma_{iT} = \left( \frac{\partial \ln \nu_i}{\partial \ln \rho} \right) = \frac{K_T}{\nu_{0i}} \left( \frac{\partial \nu_i}{\partial P} \right)_T \quad (1)$$

231 where  $\nu_{0i}$  is the mode frequency under ambient conditions,  $\rho$  is the molar density, and  
232  $K_T$  is the isothermal bulk modulus. The isothermal bulk modulus obtained for  
233 tephroite in this study is 124 GPa, and the calculated  $\gamma_{iT}$  mode Grüneisen parameters  
234 ranging from 0.3 to 1.64 are shown in Table S7.

235

## 236 **Discussion**

### 237 **Compressional behavior of tephroite**

238 The tephroite structure is described as an expanded and distorted hexagonally  
239 close-packed (hcp) array of oxygens. There are three polyhedral sites in the tephroite:  
240 Mn1O<sub>6</sub> octahedra, Mn2O<sub>6</sub> octahedra, and SiO<sub>4</sub> tetrahedra (Figure S2). The pressure  
241 dependencies of the polyhedral volumes and average bond length are shown in Figure  
242 S5 (a and b). The volumes of octahedral Mn1O<sub>6</sub> (-0.057 Å<sup>3</sup>/GPa) and Mn2O<sub>6</sub> (-0.09

243  $\text{\AA}^3/\text{GPa}$ ) and tetrahedral  $\text{SiO}_4$  ( $-0.011 \text{\AA}^3/\text{GPa}$ ) are approximately linearly compressed  
244 with increasing pressure, and the volume of  $\text{SiO}_4$  tetrahedra decreases ( $-0.011 \text{\AA}^3/\text{GPa}$ )  
245 slightly with increasing pressure. This result reflects that the compressive behavior of  
246 tephroite is mainly controlled by the  $\text{Mn1O}_6$  and  $\text{Mn2O}_6$  polyhedra. The reduction in  
247 the Mn2-O average bond length ( $-4.1\%$ ) and  $\text{Mn2O}_6$  polyhedral volume ( $-13.7\%$ ) is  
248 slightly larger than that of the Mn1-O average bond length ( $-2.8\%$ ) and  $\text{Mn1O}_6$   
249 polyhedron volume ( $-8.6\%$ ), so  $\text{Mn2O}_6$  is more compressible than  $\text{Mn1O}_6$  (Figure S5).  
250 However, the averaged bond lengths of Mn1-O and Mn2-O are equal, as are the  
251 polyhedral volumes of  $\text{Mn1O}_6$  and  $\text{Mn2O}_6$ , when an amorphization pressure of  $\sim 20$   
252 GPa is reached. In fayalite and libenbergitte, there is no phenomenon of amorphization  
253 when the average bond length (Mn1-O and Mn2-O) and polyhedral volume ( $\text{Mn1O}_6$   
254 and  $\text{Mn2O}_6$ ) are the same at  $\sim 15$  GPa and  $\sim 30$  GPa, respectively (Zhang et al. 2017,  
255 2019).

256 The degree of shortening of the Si-O bond is  $3.2\%$ , which is greater than that of  
257 Mn1-O by approximately  $2.8\%$ . For comparison, the average bond lengths of Si-O are  
258 shortened by only  $1.4\%$ ,  $1.5\%$ , and  $1.6\%$  in forsterite, fayalite, and libenbergitte,  
259 respectively (Zhang et al. 2017, 2019; Xu et al. 2020a), at the same pressure range of  
260  $\sim 20$  GPa. Due to the substitution of  $\text{Mn}^{2+}$  in olivine, the average bond lengths of  
261 Mn1-O and Mn2-O at 20 GPa cause a large change in that of Si-O, which may be a  
262 dominant factor influencing the PIA of tephroite under relatively low pressure  
263 compared with other olivines.

264 **Pressure effect on Raman spectra and vibrational modes**

265 The crystal structure of tephroite (Figure S2) represents conspicuous characteristics.  
266 The isolated SiO<sub>4</sub> tetrahedra have strong internal bonding but are distorted from the  
267 ideal T<sub>d</sub> to C<sub>s</sub> symmetry due to the static crystal-field forces and dynamic interaction  
268 between SiO<sub>4</sub> units. The bonding of Mn at M1 and M2 is much weaker than that in the  
269 SiO<sub>4</sub> tetrahedron. Therefore, the lattice vibrations of Mn cations and external SiO<sub>4</sub>  
270 occur at relatively low wavenumbers and are profoundly affected by the  
271 crystal-chemical environment in which they occur, while internal SiO<sub>4</sub> vibrations  
272 occur at high wavenumbers, between 800-1100 cm<sup>-1</sup> (Stidham et al. 1976; Hofmeister  
273 1987; Rao et al. 1988; Chopelas 1991; Kolesov and Geiger 2004).

274 The Raman spectra of tephroite are analogous to those of other end-member  
275 olivines. For example, the vibrational modes of tephroite are considered to  
276 systematically shift to frequencies 15-25 cm<sup>-1</sup> lower than the corresponding bands of  
277 forsterite (Chopelas 1991; Liu and Mernagh 1993; Kolesov and Geiger 2004; Mouri  
278 and Enami 2008), but the corresponding vibrational frequencies of transition metal  
279 olivine (Mn, Fe, Co, Ni)<sub>2</sub>SiO<sub>4</sub> are similar (Mouri and Enami 2008). In a broad sense,  
280 metal ions do not constitute an important factor controlling the relative motion of  
281 Raman-active vibrations. The approximation of the internal and external modes  
282 effectively describes these vibrations (Stidham et al. 1976). The discrepancies in  
283 Raman frequencies are caused by slightly different nonbonded atomic force constants  
284 due to lattice expansion or contraction when metal ions are replaced. The Raman  
285 spectrum of tephroite is complicated due to self-absorption (Stidham et al. 1976).  
286 More than half of the low-frequency lattice vibrations seen for forsterite and natural

287 olivine cannot be observed in this study.

288 The  $\nu_3$  mode at  $934\text{ cm}^{-1}$  shows the greatest pressure dependence of the  
289 high-frequency Ag modes of  $\text{SiO}_4$  tetrahedra (Figure 3), which is following previous  
290 studies (Chopelas 1991; Hushur et al. 2009; Liu et al. 2021). A previous study pointed  
291 out that there is a net force on Si toward O1 due to Coulomb repulsion between Si and  
292 three metallic atoms, resulting in the Si-O1 bond ( $1.62\text{ \AA}$ ) being shorter than other  
293 Si-O bonds ( $1.64\text{ \AA}$  and  $1.67\text{ \AA}$ ). Moreover,  $\nu_3$  becomes more sensitive to the volume  
294 of the M1 and M2 octahedra (Lam et al. 1990).

295 The mode Grüneisen parameters of the internal vibrational modes ( $\nu_4$ ,  $\nu_1$ , and  $\nu_3$ )  
296 range from 0.3 to 0.62 in the frequency range above  $500\text{ cm}^{-1}$  and are systematically  
297 smaller than those of 1.02-1.64 in lower-frequency lattice vibrations (Table S7). The  
298 translation of the isolated  $\text{SiO}_4$  and metallic cations is more sensitive to changes in  
299 pressure, while the Si-O bonds reflect their strong bond energy and incompressibility  
300 inside the  $\text{SiO}_4$  tetrahedra. The volume changes mainly depend on the weak bonds in  
301 the crystal structure, and the low-frequency modes associated with the weak bands are  
302 more susceptible to pressure-induced volume changes. The mode Grüneisen  
303 parameters obtained from the pressure shift of the modes are closely related. This  
304 sheds light on the compression mechanism of tephroite controlled by compression of  
305 the voids and  $\text{MnO}_6$  octahedra rather than  $\text{SiO}_4$  tetrahedra, which is consistent with  
306 the results derived from the SCXRD structural refinement.

307 Amorphous phenomena have also been observed in previous high-pressure Raman  
308 experiments on other components of olivine. Durben et al. (1993) observed two new

309 Raman bands, a relatively strong band near 825 cm<sup>-1</sup> and a weaker band at  
310 approximately 1060 cm<sup>-1</sup>, above 30 GPa in forsterite. The extrapolated ambient  
311 positions of the two new bands are 750 cm<sup>-1</sup> and 960 cm<sup>-1</sup>. It is supposed that  
312 forsterite does not experience an olivine-to-spinel conversion, but the spectral changes  
313 as a prelude to amorphization at higher pressures. On decompression, forsterite  
314 returns to its initial frequencies during the recovery of the sample under ambient  
315 conditions (Durben et al. 1993; Santamaria-Perez et al. 2016; Williams et al. 1989). In  
316 this study, after the amorphization of tephroite, the SiO<sub>4</sub> tetrahedra may collapse, but  
317 the amorphous-like phase still has a partially ordered structure, so there will be peaks  
318 near 250 cm<sup>-1</sup> and 640 cm<sup>-1</sup> positions. When the pressure is relieved, tephroite tries to  
319 restore its original structure like other component of olivine (Durben et al. 1993;  
320 Rouquette et al. 2008; Santamaria-Perez et al. 2016), and the characteristic Raman  
321 peaks of olivine at 800-840 cm<sup>-1</sup> appears. However, due to the collapse of the  
322 structure caused by the amorphization of tephroite, it is difficult to restore its initial  
323 structure of olivine after depressurization, and only the enhancement of the peak near  
324 830-840 cm<sup>-1</sup> without a complete shape. A new peak near 750 cm<sup>-1</sup> in the frequency  
325 range of typical symmetric stretching vibrations of Si-O-Si dimer linkages is observed  
326 in pyrosilicate structures and β-Mg<sub>2</sub>SiO<sub>4</sub> (Piriou and McMillan 1983; McMillan and  
327 Akaogi 1987). The formation of high-coordinate Si polyhedral species or Si-O-Si  
328 linkages formed in Si<sub>2</sub>O<sub>7</sub> dimer defects is given as the reason for the emergence of the  
329 band at 750 cm<sup>-1</sup> (Williams et al. 1989). Similar peaks also appear at frequencies of  
330 820-840 cm<sup>-1</sup> above 40 GPa for (Mg<sub>0.9</sub>Fe<sub>0.1</sub>)<sub>2</sub>SiO<sub>4</sub> that are also considered to be

331 associated with Si-O-Si linkages between pressure-induced dimerization adjacent to  
332 SiO<sub>4</sub> tetrahedra that result in fivefold- or sixfold-coordinated silicate species  
333 (Rouquette et al. 2008; Santamaria-Perez et al. 2016).

334 Additionally, four new Raman bands are detected in Ni-olivine under  
335 non-hydrostatic compression above 30 GPa, and the vibration frequencies  
336 extrapolated to zero pressure are 944 cm<sup>-1</sup>, 843 cm<sup>-1</sup>, 737 cm<sup>-1</sup>, and 235 cm<sup>-1</sup> (Lin  
337 2001). The new bands corresponding to  $\nu_0$  at 235 cm<sup>-1</sup> and 737 cm<sup>-1</sup> are close to the  $\nu_0$   
338 found at 215 cm<sup>-1</sup> and 748 cm<sup>-1</sup> for tephroite in this study, but  $\nu_0$  at 235 cm<sup>-1</sup> and 843  
339 cm<sup>-1</sup> is not observed in forsterite. It is suggested that the appearance of these new  
340 bands may indicate the formation of a new high-pressure phase, and it may also imply  
341 that irreversible amorphization of Ni-olivine occurs at higher pressure ( $P > 40$  GPa).  
342 However, the variation in the Raman bands of tephroite is different from those of  
343 forsterite and Ni-olivine. A distinct characteristic is the disappearance of the  
344 prominent vibrational frequencies of  $\nu_1+\nu_3$  at 809 cm<sup>-1</sup> and 841 cm<sup>-1</sup> as new bands  
345 appear in the Raman spectra of tephroite at 21 GPa. It indicates that the SiO<sub>4</sub>  
346 tetrahedra may collapse, but the amorphous-like phase of tephroite still has a partially  
347 ordered structure. If the pressure is increased beyond the stability field of the structure,  
348 the olivine atomic configurations are frozen and accompanied by atomic  
349 rearrangement due to saturation of the compression mechanism (Machon et al. 2014).

350 **Amorphous transformation pressure of tephroite: the lowest pressure in**  
351 **end-member olivines**

352 Tephroite undergoes PIA, as observed in both high-pressure SCXRD and Raman



353 scattering experiments in this study. Similar observations have been obtained in other  
354 end-member components of olivine in previous studies.

355 Partial amorphization of natural peridot ( $\text{Mg}_{0.88}\text{Fe}_{0.12}$ ) $_2\text{SiO}_4$  was first observed in a  
356 single crystal shock-wave experiment at approximately 56 GPa (Jeanloz et al. 1977).  
357 Fayalite glass with olivine and spinel phases was first found in laser-heated diamond  
358 anvil cell (LHDAC) experiments and was similar to that found in shocked chondritic  
359 meteorites (Lacam et al. 1980). Guyot and Reynard (1992) experimented with San  
360 Carlos olivine powder crystalline samples under high  $P$ - $T$  experiments in a LHDAC.  
361 The recovered samples were mainly amorphous when the temperature was lower than  
362 700 °C and the maximum pressure was > 70 GPa. However, the recovered samples  
363 from lower pressure (30-70 GPa) displayed a partial amorphous character and were  
364 accompanied by a hexagonally close-packed lattice (Guyot and Reynard 1992).

365 Raman spectroscopic investigation of forsterite showed that all sharp crystalline  
366 peaks disappeared at approximately 54 GPa, indicating this was the pressure of  
367 complete PIA (Santamaria-Perez et al. 2016). Recently, Kim et al. (2021) examined  
368 polycrystalline and single-crystal forsterite by *in situ* XRD measurements in  
369 laser-shocked experiments. Their results showed that the polycrystalline crystals  
370 underwent amorphization above 79 GPa, while the complete amorphous  
371 transformation of the oriented crystals occurred under higher pressure. It is worth  
372 noting that forsterite was shown to transform into an amorphous state upon  
373 decompression to ambient pressure after undergoing a high-pressure metastable  
374 transformation to forsterite III (Finkelstein et al. 2014). In contrast to the high

375 amorphous transformation pressure of forsterite, fayalite becomes amorphous at ~40  
376 GPa. Williams et al. (1990) observed the irreversible amorphous transformation of  
377 fayalite upon compression to 42 GPa by infrared spectroscopic measurements, which  
378 is believed to be associated with an increase in the coordination of silicon.  
379 Additionally, first-principles molecular dynamics simulations supported the  
380 amorphization of fayalite at 40 GPa (Misawa and Shimojo 2020), and not only  
381 sixfold- but also fivefold- coordinated silicon atoms were present in the amorphized  
382 structure under high pressures.

383 However, the amorphization pressure is significantly decreased without the use of  
384 any pressure-transmitting medium. Under these circumstances, the appearance of  
385 amorphous features in forsterite only occurs between 30-40 GPa (Durben et al. 1993;  
386 Andrault et al. 1995; Rouquette et al. 2008). In particular, for fayalite, the pressure for  
387 the appearance of amorphization is only 12 GPa (Andrault et al. 1995). Andrault et al.  
388 (1995) conducted *in situ* energy-dispersive XRD for forsterite-fayalite solid solutions.  
389 They claimed that although a wide range of amorphous features was observed at  
390 increasing pressure as the forsterite content increased, the samples still exhibited some  
391 crystalline diffraction at the highest pressures (25-59 GPa). It is worth noting that the  
392 results of Richard and Richet (1990) showed that the amorphization pressure of  
393 fayalite under non-hydrostatic conditions is similar to that in hydrostatic experiments.  
394 Additionally, new Raman bands were observed in Ni-olivine under non-hydrostatic  
395 compression above 30 GPa, suggesting that amorphization may occur at higher  
396 pressures (> 40 GPa) (Lin 2001). However, Ni-olivine still maintained its initial

397 structure and no phase transition was observed in a high-pressure SCXRD experiment  
398 up to 42.5 GPa (Zhang et al. 2019).

399 Combined with the results of the amorphization of tephroite in this study, it is  
400 evident that the amorphization pressure of olivine decreases with increasing metallic  
401 cation radius (Figure 5). Tephroite, with the largest metallic cation radius, shows the  
402 lowest pressure for amorphous transformation. Different from other components of  
403 olivine, the tephroite rapidly undergoes amorphous transformation without the  
404 original characteristics of olivine crystal. Moreover, the Raman spectra of tephroite do  
405 not return to their initial state upon decompression to ambient pressure. Compared  
406 with previous results (Durben et al. 1993; Rouquette et al. 2008; Santamaria-Perez et  
407 al. 2016), the two primary Raman peaks related to the Si-O stretching mode ( $\nu_1$  and  $\nu_3$ )  
408 reappear during the decompression process, which means the tetrahedrally bonded  
409 silicate units are restored. But this phenomenon does not appear in this paper (Figure  
410 3). Previous studies have also observed that the PIA of some materials (e.g., berlinite  
411 ( $\text{AlPO}_4$ )) returns to the initial crystalline orientation during the recovery process, the  
412 so-called memory glass effect (Meade and Jeanloz 1991). Later work showed that  
413 there is no amorphization but a distorted metastable crystalline phase, which has been  
414 proven to be a high-density crystalline phase (Gillet et al. 1995; Pellicer-Porres et al.  
415 2007).

416 The presence of the sample (single crystal or powder crystal), impurities,  
417 compression rate, and temperature are factors that lead to the amorphous  
418 transformation. (Kingma et al. 1993; Ekbundit et al. 1996; Machon et al. 2014). No

419 system can be compressed infinitely, which eventually leads to structural collapse.  
420 When structural collapse occurs at a low temperature or on a rapid timescale, ionic or  
421 atomic diffusion or bond rearrangement does not occur, resulting in a new crystalline  
422 lattice that is an amorphous solid. Amorphous material can also be formed under  
423 non-hydrostatic conditions. If the material leaves the metastable extension of its free  
424 energy curve under lower pressure and there is not sufficient thermal energy to  
425 achieve metastable crystals, the process of amorphization occurs (Machon et al. 2014;  
426 Santamaria-Perez et al. 2016). Rouquette et al. (2008) explained that the spin  
427 transition of iron leads to the amorphization of olivine within 50-75 GPa through  
428 high-pressure Mössbauer data at room temperature. The substitution of iron for  
429 magnesium in the olivine structure decreases the pressure required for saturation of  
430 the structural compression. Therefore, the reduction in the iron ionic radius ( $r_{\text{Fe}^{2+}(\text{HS})}$   
431 = 78 pm and  $r_{\text{Fe}^{2+}(\text{LS})}$  = 61 pm) after spin transition causes a local collapse of the  
432 structure, resulting in a downshift in the pressure of the amorphous transition. This  
433 phenomenon is in contrast to the results of this study in that the amorphization  
434 pressure decreases with increasing ionic radius. The larger Mn ionic radius results in a  
435 lower amorphous transition pressure. The amorphization pressures of forsterite,  
436 fayalite, and tephroite show a downward trend with increasing metal ion radius.  
437 Therefore, Ni-olivine transforms into an amorphous state under higher pressure than  
438 forsterite. The substitution of iron or Mn ions for magnesium ions may reduce the  
439 local energetic barriers and further affect the structural transformation kinetics  
440 (Santamaria-Perez et al. 2016).

441

## 442 **Geophysical Implication**

443 The Mn-rich mineral inclusions found in ophiolite-host diamonds are speculated to  
444 have originated at a depth of 200-250 km and to be related to the early subducted  
445 normal Mid-ocean ridge basalts (MORB) with a 10% ferromanganese crustal  
446 composition. These Mn-rich minerals included in diamonds are mainly Ni-Mn-Co  
447 alloys, Mn silicate (*e.g.* Mn, Ca silicate with an orthorhombic perovskite structure,  
448 tephroite, and spessartine), and MnO (Robinson et al. 2015; Moe et al. 2017; Lian et  
449 al. 2018; Lian and Yang 2019; Wu et al. 2019). A proportion of Mn-nodules and  
450 Mn-bearing sediments are distributed at the bottom of the ocean (Verlaan et al. 2004),  
451 which are in the subducted slab before the formation of the ophiolite.

452 The SCXRD and Raman spectroscopy experiments in this study confirm that  
453 tephroite undergoes an amorphous transformation at ~900 K and ~20 GPa (Figure 6a).  
454 The amorphous phase cannot return to the original olivine structure after cooling and  
455 depressurization. Moreover, unlike forsterite and fayalite, a previous study observed  
456 that tephroite decomposed into MnO plus MnSiO<sub>3</sub> at ~14 GPa and ~1273 K and  
457 further decomposed into MnO plus SiO<sub>2</sub> at ~30 GPa (Ito et al. 1974). Mn-nodules are  
458 thought to be distributed at the bottom of the oceanic crust (Verlaan et al. 2004) and  
459 the high density of tephroite promotes the subduction of slab into Earth's interior.  
460 There is a situation if an ancient oceanic slab with lower temperatures subducts  
461 rapidly (*e.g.*, Tonga slab with a center temperature of 800 K at 600 km (Bina and  
462 Navrotsky 2000; Ganguly et al. 2009)), amorphous tephroite would appear as the slab

463 subducts into the transition zone and even deeper. In addition, amorphous olivine may  
464 cause grain boundary flow, which enhances sliding and causes a significant decrease  
465 in viscosity (Samae et al. 2021). The low viscosity of amorphous tephroite and  
466 metastable olivine and pyroxene (Xu et al. 2020b) may be the possible factors  
467 resulting in the stagnation of the cold slab in the transition zone. Therefore, tephroite  
468 may exist in stagnant slabs as an amorphous phase. However, for the subducting slab  
469 with higher temperature, tephroite may be decomposed into MnO and MnSiO<sub>3</sub> under  
470 high pressure and high temperature, and even continue to decompose into MnO and  
471 SiO<sub>2</sub>.

472 Ample evidence suggests that crustal materials that are subducted into the deep  
473 Earth can be brought back to the surface through mantle convection or mantle plumes  
474 (Xiong et al. 2015; Yang et al. 2015b). Figure 17 in Yang et al. (2015a) shows that  
475 tephroite is surrounded by MnO, Mn-garnet, and (Ni, Co)<sub>3</sub>Mn in ophiolite-hosted  
476 diamonds. There may be a situation where the low-viscosity amorphous tephroite is  
477 more likely to be wrapped in the alloy melt (Figure 6). During rapid uplift (Howell et  
478 al. 2015; McGowan et al. 2015), the carbon in the alloy melt is quickly exsolved as  
479 diamond (Sokol et al. 2009). Under the impact of high temperature, the diamond  
480 grows, and the amorphous tephroite recrystallizes and further decomposes into MnO  
481 and Mn-garnet. The resulting products then encased the recrystallized tephroite. In  
482 another possible situation, the amorphous tephroite crystallized under the influence of  
483 high temperature before being wrapped by diamond and further decomposed during  
484 transportation. Therefore, the state of tephroite at higher temperatures needs to be

485 constrained by more experiments. Mixtures of UHP, highly reduced minerals, and  
486 crustal materials coexist in ophiolitic peridotites and chromitites far from their normal  
487 stability fields (Robinson et al. 2015; Yang et al. 2015a, 2015b), indicating that their  
488 formation is multistage and that UHP and highly reduced minerals are formed in the  
489 deep mantle.

490 The mineral inclusions in diamonds provide a good window for understanding the  
491 deep cycling of oceanic crustal materials and the composition of the deep mantle.  
492 Tephroite can exist in an amorphous form in a stagnant slab at the transition zone and  
493 even in the lower mantle. Amorphous tephroite or some other amorphous substances  
494 would profoundly influence the distribution of elements, transparency properties, and  
495 kinetic properties in the Earth's interior. Further works are of vital importance to  
496 discussing the amorphous phase in the system and may be able to elucidate deep  
497 crustal material recycling.

498

#### 499 **Data availability**

500 All data generated or analyzed during this study are included in this published article  
501 and its Supplementary Information files.

#### 502 **Author contributions**

503 Z.Y., J.X., and D.F. designed the project. Z.Y., J.X., D.F., D.Z., W.Z., and H.X.  
504 participated in the data collection and analysis. Z.Y., and J.X. were responsible for  
505 data interpretation and wrote the manuscript. D.F., D.Z., W.Z., and H.X. participated  
506 in the discussion and provided comments on the manuscript.

507 **Competing interests:** The authors declare no competing interests.

508

509 **Acknowledgments**

510 This project was funded by the National Natural Science Foundation of China (Grant  
511 Nos. 42172048, U2032118 and 41802043), the Youth Innovation Promotion  
512 Association CAS (Dawei Fan, 2018434), the Chinese Academy of Sciences “Light of  
513 West China” Program (2019), the Guizhou Provincial Science and Technology  
514 Projects (QKHJC-ZK[2021]ZD042). The experiments were performed at  
515 GeoSoilEnviroCARS (13-BM-C), Advanced Photon Source (APS), and Argonne  
516 National Laboratory. The use of the gas-loading system is supported by COMPRES  
517 and GeoSoilEnviroCARS. GeoSoilEnviroCARS is supported by the National Science  
518 Foundation—Earth Sciences (EAR-1634415) and the Department of  
519 Energy—Geosciences (DE-FG02-94ER14466). COMPRES is under NSF  
520 Cooperative Agreement EAR-1661511. Use of the Advanced Photon Source was  
521 supported by the U.S. Department of Energy, Office of Science, Office of Basic  
522 Energy Sciences, under Contract No. DE-AC02-06CH11357. We acknowledge  
523 Sergey N. Tkachev and Bin Yang for gas loading assistances. The authors declare no  
524 competing financial interests.

525

526 **References:**

527 Andrault, D., Bouhifd, M.A., Itie, J.P., Richet, P., Itie, J.P., and Richet, P. (1995)  
528 Compression and amorphization of  $(\text{Mg,Fe})_2\text{SiO}_4$  olivines: An X-ray diffraction  
529 study up to 70 GPa. *Physics and Chemistry of Minerals*, 22, 99–107.



- 530 Angel, R.J., Alvaro, M., and Gonzalez-Platas, J. (2014) EosFit7c and a Fortran  
531 module (library) for equation of state calculations. *Zeitschrift für*  
532 *Kristallographie - Crystalline Materials*, 229.
- 533 Bina, C.R., and Navrotsky, A. (2000) Possible presence of high-pressure ice in cold  
534 subducting slabs. *Nature*, 408, 844–847.
- 535 Birch, F. (1947) Finite Elastic Strain of Cubic Crystals. *Physical Review*, 71,  
536 809–824.
- 537 Chopelas, A. (1991) Single crystal Raman spectra of forsterite, fayalite, and  
538 monticellite. *American Mineralogist*, 76, 1101–1109.
- 539 Cloutis, E.A. (1997) Mn-rich olivines: Identification from spectral reflectance  
540 properties. *Journal of Geophysical Research: Planets*, 102, 25575–25580.
- 541 Dolomanov, O. V., Bourhis, L.J., Gildea, R.J., Howard, J.A.K., and Puschmann, H.  
542 (2009) OLEX2 : a complete structure solution, refinement and analysis program.  
543 *Journal of Applied Crystallography*, 42, 339–341.
- 544 Durben, D.J., McMillan, P.F., and Wolf, G.H. (1993) Raman study of the  
545 high-pressure behavior of forsterite ( $\text{Mg}_2\text{SiO}_4$ ) crystal and glass. *American*  
546 *Mineralogist*, 78, 1143–1148.
- 547 Ekbundit, S., Leinenweber, K., Yarger, J.L., Robinson, J.S., Verhelst-Voorhees, M.,  
548 and Wolf, G.H. (1996) New High-Pressure Phase and Pressure-Induced  
549 Amorphization of  $\text{Ca}(\text{OH})_2$ : Grain Size Effect. *Journal of Solid State Chemistry*,  
550 126, 300–307.
- 551 Fei, Y. (1995) Thermal Expansion. In *Mineral Physics & Crystallography: A*

- 552 Handbook of Physical Constants pp. 29–44.
- 553 Fei, Y., Ricolleau, A., Frank, M., Mibe, K., Shen, G., and Prakapenka, V. (2007)
- 554 Toward an internally consistent pressure scale. Proceedings of the National
- 555 Academy of Sciences, 104, 9182–9186.
- 556 Finkelstein, G.J., Dera, P.K., Jahn, S., Oganov, A.R., Holl, C.M., Meng, Y., and
- 557 Duffy, T.S. (2014) Phase transitions and equation of state of forsterite to 90 GPa
- 558 from single-crystal X-ray diffraction and molecular modeling. American
- 559 Mineralogist, 99, 35–43.
- 560 Frost, D.J. (2008) The Upper Mantle and Transition Zone. Elements, 4, 171–176.
- 561 Fujino, K., Sasaki, S., Takéuchi, Y., and Sadanaga, R. (1981) X-ray determination of
- 562 electron distributions in forsterite, fayalite and tephroite. Acta Crystallographica
- 563 Section B Structural Crystallography and Crystal Chemistry, 37, 513–518.
- 564 Gaillard, F., Scaillet, B., Pichavant, M., and Iacono-Marziano, G. (2015) The redox
- 565 geodynamics linking basalts and their mantle sources through space and time.
- 566 Chemical Geology, 418, 217–233.
- 567 Ganguly, J., Freed, A.M., and Saxena, S.K. (2009) Density profiles of oceanic slabs
- 568 and surrounding mantle: Integrated thermodynamic and thermal modeling, and
- 569 implications for the fate of slabs at the 660 km discontinuity. Physics of the
- 570 Earth and Planetary Interiors, 172, 257–267.
- 571 Geiger, C.A., Grodzicki, M., and Dachs, E. (2019) An analysis of the magnetic
- 572 behavior of olivine and garnet substitutional solid solutions. American
- 573 Mineralogist, 104, 1246–1255.

- 574 Gillet, P., and Guyot, F. (1988) High pressure-high temperature Raman spectroscopy  
575 of Ca<sub>2</sub>GeO<sub>4</sub> (olivine form): Some insights on anharmonicity. Chemical Geology,  
576 70, 61.
- 577 Gillet, P., Badro, J., Varrel, B., and McMillan, P.F. (1995) High-pressure behavior in  
578  $\alpha$ -AlPO: Amorphization and the memory-glass effect. Physical Review B, 51,  
579 11262–11269.
- 580 Guyot, F., and Reynard, B. (1992) Pressure-induced structural modifications and  
581 amorphization in olivine compounds. Chemical Geology, 96, 411–420.
- 582 Hofmeister, A.M. (1987) Single-crystal absorption and reflection infrared  
583 spectroscopy of forsterite and fayalite. Physics and Chemistry of Minerals, 14,  
584 499–513.
- 585 Howell, D., Griffin, W.L., Yang, J., Gain, S., Stern, R.A., Huang, J.-X., Jacob, D.E.,  
586 Xu, X., Stokes, A.J., O'Reilly, S.Y., and others (2015) Diamonds in ophiolites:  
587 Contamination or a new diamond growth environment? Earth and Planetary  
588 Science Letters, 430, 284–295.
- 589 Hushur, A., Manghnani, M.H., Smyth, J.R., Nestola, F., and Frost, D.J. (2009) Crystal  
590 chemistry of hydrous forsterite and its vibrational properties up to 41 GPa.  
591 American Mineralogist, 94, 751–760.
- 592 Ito, E., Matsumoto, T., and Kawai, N. (1974) High-pressure decompositions in Mn  
593 silicates and their geophysical implications. Physics of the Earth and Planetary  
594 Interiors, 8, 241–245.
- 595 Jeanloz, R., Ahrens, T.J., Lally, J.S., Nord, G.L., Christie, J.M., and Heuer, A.H.

- 596 (1977) Shock-Produced Olivine Glass: First Observation. *Science*, 197, 457–459.
- 597 Kim, D., Tracy, S.J., Smith, R.F., Gleason, A.E., Bolme, C.A., Prakapenka, V.B.,  
598 Appel, K., Speziale, S., Wicks, J.K., Berryman, E.J., and others (2021)  
599 Femtosecond X-Ray Diffraction of Laser-Shocked Forsterite ( $\text{Mg}_2\text{SiO}_4$ ) to 122  
600 GPa. *Journal of Geophysical Research: Solid Earth*, 126, 1–14.
- 601 Kingma, K.J., Hemley, R.J., Mao, H., and Veblen, D.R. (1993) New high-pressure  
602 transformation in  $\alpha$ -quartz. *Physical Review Letters*, 70, 3927–3930.
- 603 Kolesov, B.A., and Geiger, C.A. (2004) A Raman spectroscopic study of Fe-Mg  
604 olivines. *Physics and Chemistry of Minerals*, 31, 142–154.
- 605 Lacam, A., Madon, M., and Poirier, J.P. (1980) Olivine glass and spinel formed in a  
606 laser heated, diamond-anvil high pressure cell. *Nature*, 288, 155–157.
- 607 Lam, P.K., Yu, R., Lee, M.W., and Sharma, S.K. (1990) Structural distortions and  
608 vibrational modes in  $\text{Mg}_2\text{SiO}_4$ . *American Mineralogist*, 75, 109–119.
- 609 Lian, D., and Yang, J. (2019) Ophiolite-Hosted Diamond: A New Window for  
610 Probing Carbon Cycling in the Deep Mantle. *Engineering*, 5, 406–420.
- 611 Lian, D., Yang, J., Wiedenbeck, M., Dilek, Y., Rocholl, A., and Wu, W. (2018)  
612 Carbon and nitrogen isotope, and mineral inclusion studies on the diamonds from  
613 the Pozanti–Karsanti chromitite, Turkey. *Contributions to Mineralogy and  
614 Petrology*, 173, 72.
- 615 Lin, C.C. (2001) High-pressure Raman spectroscopic study of Co- and Ni-olivines.  
616 *Physics and Chemistry of Minerals*, 28, 249–257.
- 617 Liu, D., Guo, X., Smyth, J.R., Wang, X., Zhu, X., Miao, Y., Bai, J., and Ye, Y. (2021)

618 High-temperature and high-pressure Raman spectra of Fo<sub>89</sub>Fa<sub>11</sub> and Fo<sub>58</sub>Fa<sub>42</sub>  
619 olivines: Iron effect on thermodynamic properties. *American Mineralogist*, 106,  
620 1668–1678.

621 Liu, L.-G., and Mernagh, T.P. (1993) Raman spectra of forsterite and fayalite at high  
622 pressures and room temperature. *High Pressure Research*, 11, 241–256.

623 Machon, D., Meersman, F., Wilding, M.C., Wilson, M., and McMillan, P.F. (2014)  
624 Pressure-induced amorphization and polyamorphism: Inorganic and biochemical  
625 systems. *Progress in Materials Science*, 61, 216–282.

626 Mao, H.K., Xu, J., and Bell, P.M. (1986) Calibration of the ruby pressure gauge to  
627 800 kbar under quasi-hydrostatic conditions. *Journal of Geophysical Research*,  
628 91, 4673.

629 Mason, B. (1963) Olivine composition in chondrites. *Geochimica et Cosmochimica*  
630 *Acta*, 27, 1011–1023.

631 McGowan, N.M., Griffin, W.L., González-Jiménez, J.M., Belousova, E., Afonso, J.C.,  
632 Shi, R., McCammon, C.A., Pearson, N.J., and O'Reilly, S.Y. (2015) Tibetan  
633 chromitites: Excavating the slab graveyard. *Geology*, 43, 179–182.

634 McMillan, P., and Akaogi, M. (1987) Raman spectra of  $\beta$ -Mg<sub>2</sub>SiO<sub>4</sub> (modified spinel)  
635 and  $\gamma$ -Mg<sub>2</sub>SiO<sub>4</sub> (spinel). *American Mineralogist*, 72, 361–364.

636 Meade, C., and Jeanloz, R. (1991) Deep-Focus Earthquakes and Recycling of Water  
637 into the Earth's Mantle. *Science*, 252, 68–72.

638 Misawa, M., and Shimojo, F. (2020) First-Principles Study of Pressure-Induced  
639 Amorphization of Fe<sub>2</sub>SiO<sub>4</sub> Fayalite. *physica status solidi (b)*, 257, 2000173.

- 640 Moe, K.S., Yang, J.-S., Johnson, P., Xu, X., and Wang, W. (2017) Spectroscopic  
641 analysis of microdiamonds in ophiolitic chromitite and peridotite. *Lithosphere*,  
642 L603.1.
- 643 Momma, K. & Izumi, F. (2011) VESTA 3 for three-dimensional visualization of  
644 crystal, volumetric and morphology data. *Journal of Applied Crystallography* 44,  
645 1272-1276.
- 646 Mouri, T., and Enami, M. (2008) Raman spectroscopic study of olivine-group  
647 minerals. *Journal of Mineralogical and Petrological Sciences*, 103, 100–104.
- 648 Mustard, J.F., Poulet, F., Gendrin, A., Bibring, J.-P., Langevin, Y., Gondet, B.,  
649 Mangold, N., Bellucci, G., and Altieri, F. (2005) Olivine and Pyroxene Diversity  
650 in the Crust of Mars. *Science*, 307, 1594–1597.
- 651 Nguyen, A.N., and Zinner, E. (2004) Discovery of Ancient Silicate Stardust in a  
652 Meteorite. *Science*, 303, 1496–1499.
- 653 Pellicer-Porres, J., Saitta, A.M., Polian, A., Itié, J.P., and Hanfland, M. (2007)  
654 Six-fold-coordinated phosphorus by oxygen in  $\text{AlPO}_4$  quartz homeotype under  
655 high pressure. *Nature Materials*, 6, 698–702.
- 656 Piriou, B., and McMillan, P. (1983) The high-frequency vibrational spectra of  
657 vitreous and crystalline orthosilicates. *American Mineralogist*, 68, 426–443.
- 658 Rao, K.R., Chaplot, S.L., Choudhury, N., Ghose, S., Hastings, J.M., Corliss, L.M.,  
659 and Price, D.L. (1988) Lattice dynamics and inelastic neutron scattering from  
660 forsterite,  $\text{Mg}_2\text{SiO}_4$ : Phonon dispersion relation, density of states and specific  
661 heat. *Physics and Chemistry of Minerals*, 16.

- 662 Richard, G., and Richet, P. (1990) Room-temperature amorphization of fayalite and  
663 high-pressure properties of Fe<sub>2</sub>SiO<sub>4</sub> liquid. *Geophysical Research Letters*, 17,  
664 2093–2096.
- 665 Ringwood, A.E. (1991) Phase transformations and their bearing on the constitution  
666 and dynamics of the mantle. *Geochimica et Cosmochimica Acta*, 55, 2083–2110.
- 667 Rivers, M., Prakapenka, V., Kubo, A., Pullins, C., Holl, C., and Jacobsen, S. (2008)  
668 The COMPRES/GSECARS gas-loading system for diamond anvil cells at the  
669 Advanced Photon Source. *High Pressure Research*, 28, 273–292.
- 670 Robinson, P.T., Trumbull, R.B., Schmitt, A., Yang, J.-S., Li, J.-W., Zhou, M.-F.,  
671 Erzinger, J., Dare, S., and Xiong, F. (2015) The origin and significance of crustal  
672 minerals in ophiolitic chromitites and peridotites. *Gondwana Research*, 27,  
673 486–506.
- 674 Rouquette, J., Kantor, I., McCammon, C.A., Dmitriev, V., and Dubrovinsky, L.S.  
675 (2008) High-Pressure Studies of (Mg<sub>0.9</sub>Fe<sub>0.1</sub>)<sub>2</sub>SiO<sub>4</sub> Olivine Using Raman  
676 Spectroscopy, X-ray Diffraction, and Mössbauer Spectroscopy. *Inorganic  
677 Chemistry*, 47, 2668–2673.
- 678 Samae, V., Cordier, P., Demouchy, S., Bollinger, C., Gasc, J., Koizumi, S., Mussi, A.,  
679 Schryvers, D., and Idrissi, H. (2021) Stress-induced amorphization triggers  
680 deformation in the lithospheric mantle. *Nature*, 591, 82–86.
- 681 Santamaria-Perez, D., Thomson, A., Segura, A., Pellicer-Torres, J., Manjon, F.J.,  
682 Cora, F., McColl, K., Wilson, M., Dobson, D., and McMillan, P.F. (2016)  
683 Metastable structural transformations and pressure-induced amorphization in

- 684 natural (Mg,Fe)<sub>2</sub>SiO<sub>4</sub> olivine under static compression: A raman spectroscopic  
685 study. *American Mineralogist*, 101, 1642–1650.
- 686 Sheldrick, G.M. (2008) A short history of SHELX. *Acta Crystallographica Section A*  
687 *Foundations of Crystallography*, 64, 112–122.
- 688 Sokol, A.G., Palyanova, G.A., Palyanov, Y.N., Tomilenko, A.A., and Melenevsky,  
689 V.N. (2009) Fluid regime and diamond formation in the reduced mantle:  
690 Experimental constraints. *Geochimica et Cosmochimica Acta*, 73, 5820–5834.
- 691 Speziale, S., Duffy, T.S., and Angel, R.J. (2004) Single-crystal elasticity of fayalite to  
692 12 GPa. *Journal of Geophysical Research: Solid Earth*, 109, 1–15.
- 693 Stidham, H.D., Bates, J.B., and Finch, C.B. (1976) Vibrational spectra of synthetic  
694 single crystal tephroite, Mn<sub>2</sub>SiO<sub>4</sub>. *The Journal of Physical Chemistry*, 80,  
695 1226–1234.
- 696 Verlaan, P.A., Cronan, D.S., and Morgan, C.L. (2004) A comparative analysis of  
697 compositional variations in and between marine ferromanganese nodules and  
698 crusts in the South Pacific and their environmental controls. *Progress in*  
699 *Oceanography*, 63, 125–158.
- 700 Williams, Q., McMillan, P., and Cooney, T. (1989) Vibrational spectra of olivine  
701 composition glasses: The Mg-Mn join. *Physics and Chemistry of Minerals*, 16,  
702 352–359.
- 703 Williams, Q., Knittle, E., Reichlin, R., Martin, S., and Jeanloz, R. (1990) Structural  
704 and electronic properties of Fe<sub>2</sub>SiO<sub>4</sub>-fayalite at ultrahigh pressures:  
705 amorphization and gap closure. *Journal of Geophysical Research*, 95, 549–563.



- 706 Wu, W., Yang, J., Wirth, R., Zheng, J., Lian, D., Qiu, T., and Milushi, I. (2019)  
707 Carbon and nitrogen isotopes and mineral inclusions in diamonds from  
708 chromitites of the Mirdita ophiolite (Albania) demonstrate recycling of oceanic  
709 crust into the mantle. *American Mineralogist*, 104, 485–500.
- 710 Xiong, F., Yang, J., Robinson, P.T., Xu, X., Liu, Z., Li, Y., Li, J., and Chen, S. (2015)  
711 Origin of podiform chromitite, a new model based on the Luobusa ophiolite,  
712 Tibet. *Gondwana Research*, 27, 525–542.
- 713 Xu, J., Fan, D., Zhang, D., Li, B., Zhou, W., and Dera, P.K. (2020a) Investigation of  
714 the crystal structure of a low water content hydrous olivine to 29.9 GPa: A  
715 high-pressure single-crystal X-ray diffraction study. *American Mineralogist*, 105,  
716 1857–1865.
- 717 Xu, J., Fan, D., Zhang, D., Guo, X., Zhou, W., and Dera, P.K. (2020b) Phase  
718 transition of enstatite-ferrosilite solid solutions at high pressure and high  
719 temperature: constraints on metastable orthopyroxene in cold subduction.  
720 *Geophysical Research Letters*, 47, 1–10.
- 721 Yang, J., Robinson, P.T., and Dilek, Y. (2015a) Diamond-bearing ophiolites and their  
722 geological occurrence. *Episodes*, 38, 344–364.
- 723 Yang, J., Meng, F., Xu, X., Robinson, P.T., Dilek, Y., Makeyev, A.B., Wirth, R.,  
724 Wiedenbeck, M., and Cliff, J. (2015b) Diamonds, native elements and metal  
725 alloys from chromitites of the Ray-Iz ophiolite of the Polar Urals. *Gondwana*  
726 *Research*, 27, 459–485.
- 727 Ye, Z., Fan, D., Tang, Q., Xu, J., Zhang, D., and Zhou, W. (2021) Constraining the

- 728 density evolution during destruction of the lithospheric mantle in the eastern  
729 North China Craton. *Gondwana Research*, 91, 18–30.
- 730 Zhang, D., Hu, Y., Xu, J., Downs, R.T., Hammer, J.E., and Dera, P.K. (2019)  
731 High-pressure behavior of liebenbergite: The most incompressible  
732 olivine-structured silicate. *American Mineralogist*, 104, 580–587.
- 733 Zhang, J.S., Hu, Y., Shelton, H., Kung, J., and Dera, P. (2017) Single-crystal X-ray  
734 diffraction study of Fe<sub>2</sub>SiO<sub>4</sub> fayalite up to 31 GPa. *Physics and Chemistry of*  
735 *Minerals*, 44, 171–179.
- 736 Zolensky, M.E., Zega, T.J., Yano, H., Wirick, S., Westphal, A.J., Weisberg, M.K.,  
737 Weber, I., Warren, J.L., Velbel, M.A., Tsuchiyama, A., and others (2006)  
738 Mineralogy and Petrology of Comet 81P/Wild 2 Nucleus Samples. *Science*, 314,  
739 1735–1739.

Figure:

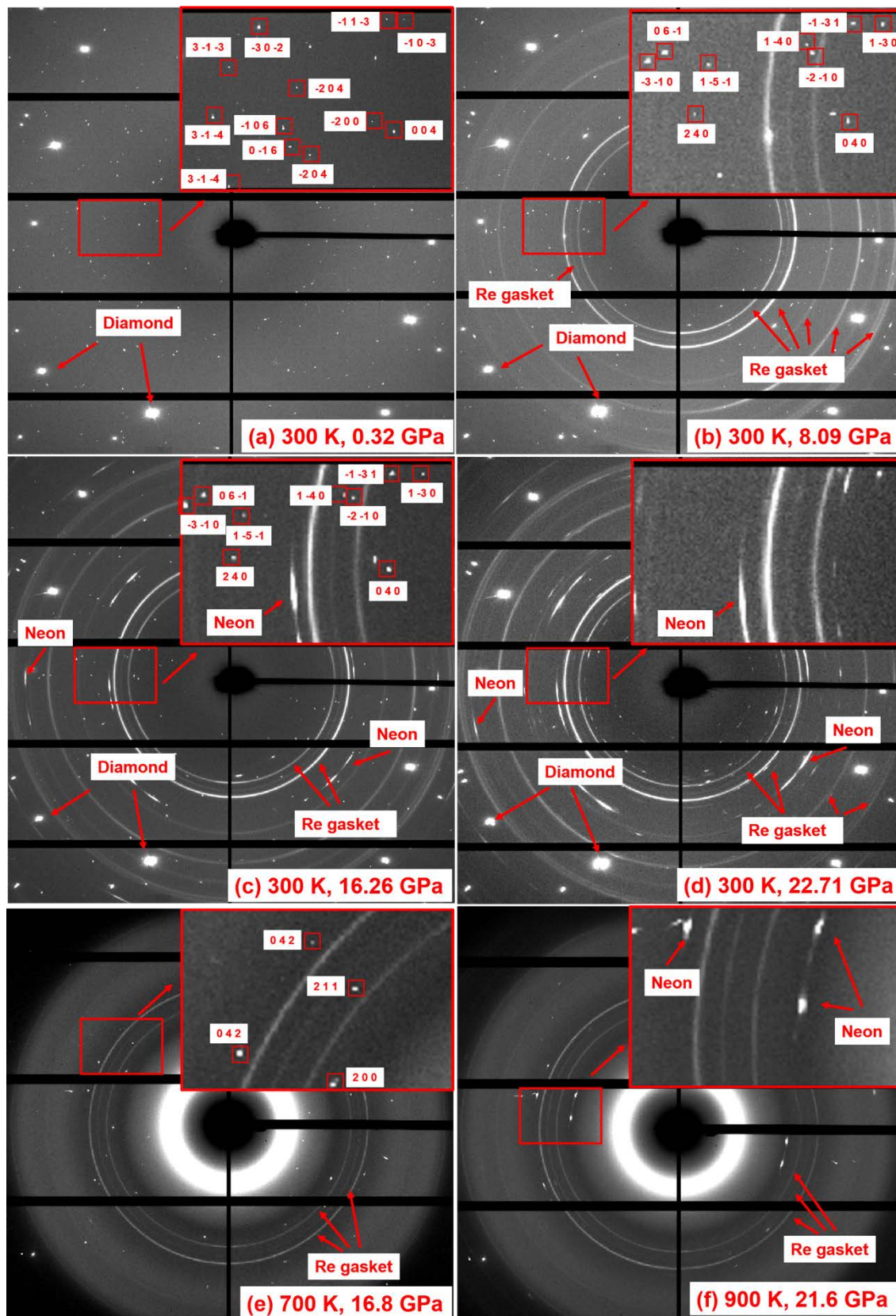
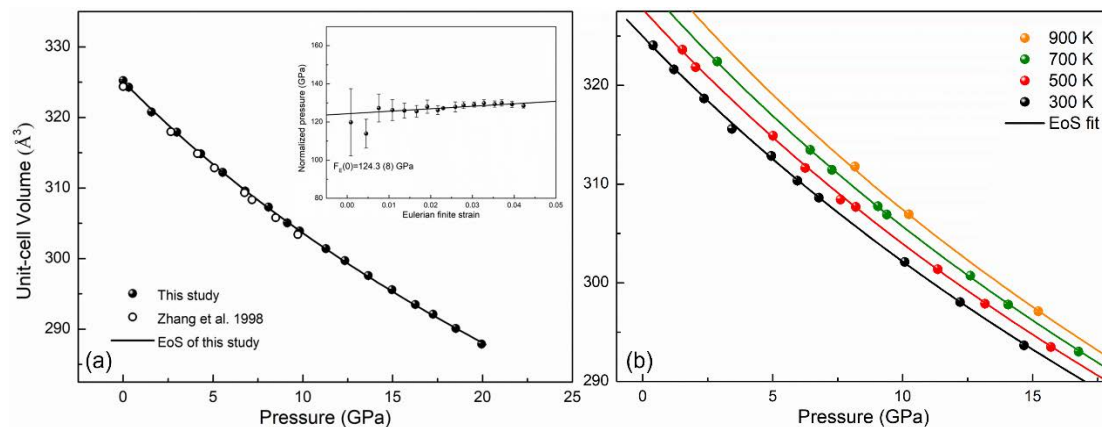
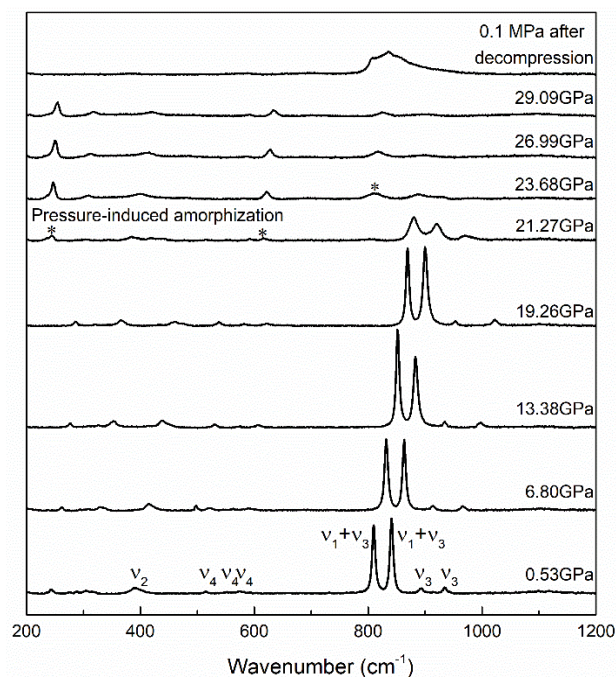


Figure 1. Single-crystal X-ray diffraction patterns of tephroite at different pressure

and temperature conditions. The Miller indices of selected diffraction peaks are also shown for each phase at specific pressures. Sharp crystalline diffraction peaks appear after 20 GPa. All new closed rings are identified to Re gasket.



**Figure 2.** (a) Unit-cell volume compression curve of tephroite and the best-fit BM3 equation of state. Inset: Eulerian finite strain-normalized pressure ( $F_E - f_E$ ) plot of tephroite. The solid lines represent the linear fit to the data. (b) Pressure-volume-temperature relationships of tephroite. The isothermal compression curves are calculated with the thermal EoS parameters obtained in this study.



**Figure 3.** Representative room-temperature Raman scattering spectra of tephroite obtained in this study up to 29.09 GPa on the stroke and after decompression to 0.1 MPa. Asterisks (\*) represent new peaks.

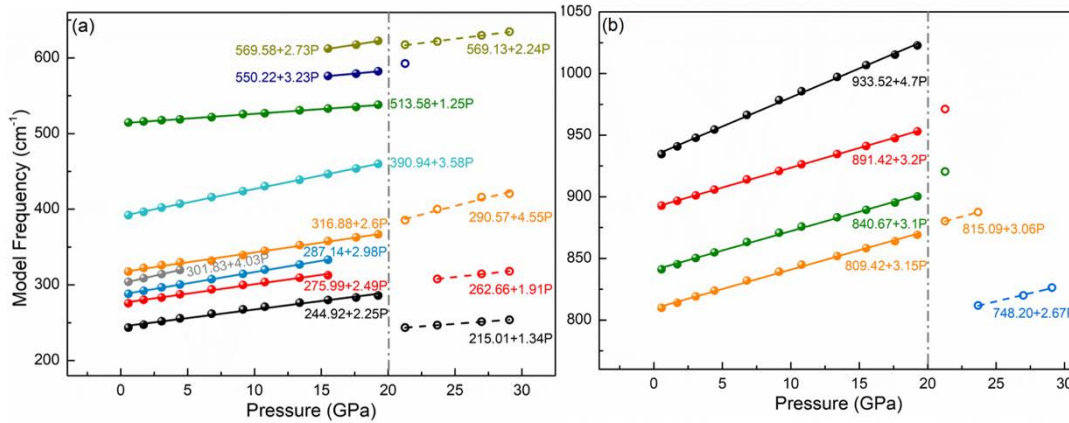


**Figure 4.** Pressure dependence of the Raman-active modes for tephroite in the frequency ranges of (a) 180-660 cm<sup>-1</sup> and (b) 700-1050 cm<sup>-1</sup>, with linear regression for each vibrational data set.

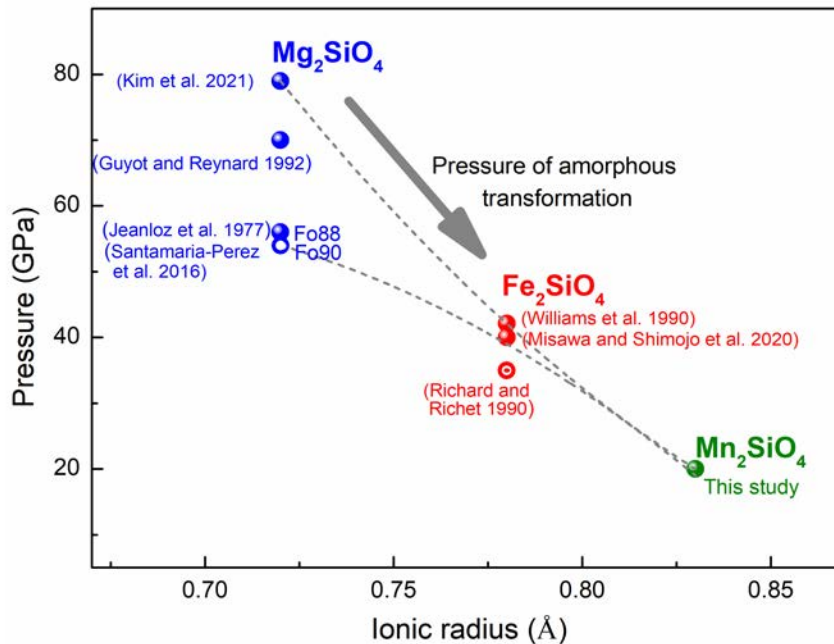


**Figure 5.** Amorphous transformation pressure of end-member olivine (Mg, Fe, Mn)<sub>2</sub>SiO<sub>4</sub> with ionic radius. The amorphization pressure of olivine from previous

studies is shown for comparison (Jeanloz et al. 1977; Williams et al. 1990; Richard and Richet 1990; Guyot and Reynard 1992; Santamaria-Perez et al. 2016; Misawa and Shimojo 2020; Kim et al. 2021). The solid circles indicate a mixture of crystalline and amorphous phases, hollow circles represent the complete amorphous pressure, and the points inside the hollow circles represent the pressure at which the samples are partially amorphous. The gray dashed curves represent the polynomial fits.

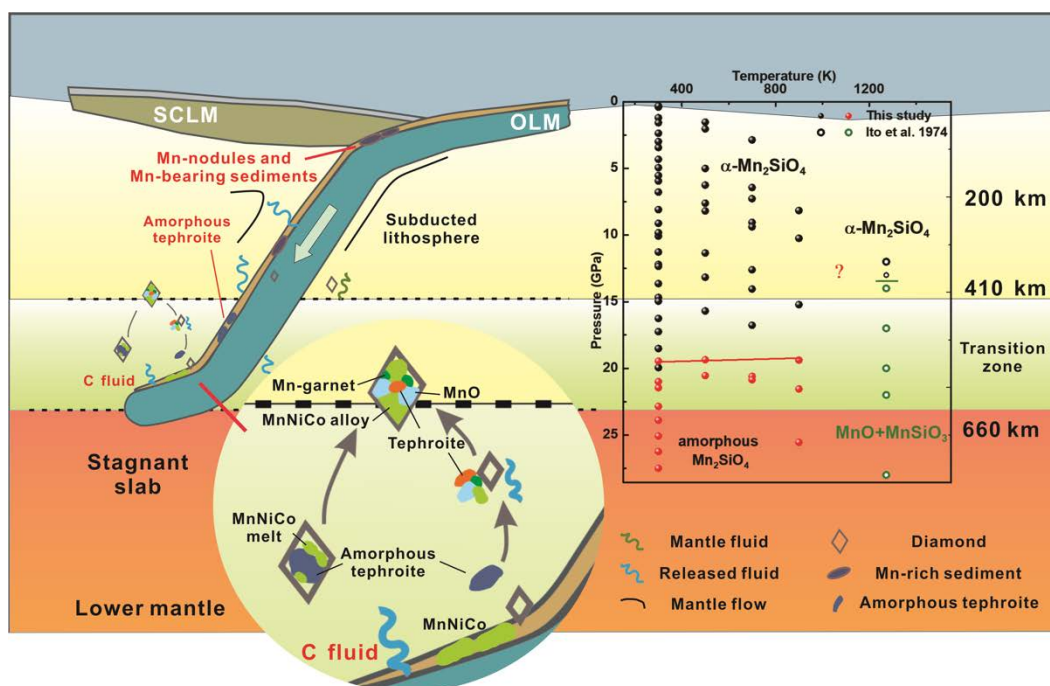


**Figure 6.** Schematic graph of diamond formation with tephroite. Subduction brings the Mn-bearing oceanic crustal assemblage into the Earth's interior. The slab subducts to the transition zone with a partially metal alloy melt, which further evolves into a MnNiCo alloy melt. The buoyant material returns to shallow depths during rapid uplift. In the process of the uplift and growth of diamonds, some of the alloy melt and some of the high-density materials are included. Phase diagram of tephroite under high  $P$ - $T$  conditions. The black and red solid circles represent  $\alpha$ -tephroite and amorphous tephroite in this study, respectively. The black and green hollow points are

$\alpha$ -tephroite and decomposition products of MnO and MnSiO<sub>3</sub> (tetragonal garnet),  
respectively.